Preparation and characterisation of iron substituted $Mn_{1.7}Cu_{1.3-x}Fe_xO_4$ spinel oxides (x= 0, 0.1, 0.3, 0.5)

Justyna Ignaczak[1*], Yevgeniy Naumovich[2], Karolina Górnicka[3], Jan Jamroz[4], Wojciech Wróbel[4], Jakub Karczewski[3], Ming Chen[5], Piotr Jasiński[1], Sebastian Molin[1]

[1] Faculty of Electronics, Telecommunications and Informatics, Gdańsk University of Technology,
ul. G. Narutowicza 11/12, 80-233 Gdańsk, Poland
[2] Department of High Temperature Electrochemical Processes, Institute of Power Engineering,
ul. Augustówka 36, 02-981 Warsaw, Poland
[3] Faculty of Applied Physics and Mathematics, Gdańsk University of Technology,
ul. G. Narutowicza 11/12, 80-233 Gdańsk, Poland
[4] Faculty of Physics, Warsaw University of Technology, ul. Koszykowa 75, 00-662 Warsaw, Poland

[5] Department of Energy Conversion and Storage, Technical University of Denmark, Fysikvej, 2800 Kgs. Lyngby, Denmark

*corresponding author: justyna.ignaczak@pg.edu.pl

Abstract

Spinel oxides with the general formula $Mn_{1.7}Cu_{1.3-x}Fe_xO_4$ (x= 0, 0.1, 0.3, 0.5) were prepared and evaluated in this work for their properties at high temperatures. The effect of partially substituting Cu by Fe has not been studied so far for this group of materials and is thus evaluated in this work.

$Mn_{1.7}Cu_{1.3-x}Fe_xO_4$ powders were synthesised by a soft chemistry process and studied in terms of crystallographic phase analysis, electrical conductivity, thermal expansion, and sinterability behaviour. The results show that the Fe content has a significant influence on the phase composition and the resulting properties. Characterisation of the dilatometry and conductivity coupled with XRD phase analysis across a wide temperature range allowed the relations between the materials properties and compositions to be observed. The results indicate that $Mn_{1.7}Cu_{0.8}Fe_{0.5}O_4$is a promising material for use as a protective coating for interconnects in intermediate temperature Solid Oxide Fuel Cells.

Introduction

Spinel oxides form a remarkable group of ceramic materials with a wide range of potential applications [1]. The general formula of a “regular” spinel is AB_2O_4 with either a cubic or tetragonal structure, where A is a divalent cation, and B is a trivalent cation, which occupy tetrahedral and octahedral sites, respectively. The spinel mineral is $MgAl_2O_4$, which has a regular structure. A spinel can also adopt an “inverse” structure, where half of the trivalent B cations occupy the tetrahedral sites, and the divalent A cations and the remaining half of the B cations occupy the octahedral sites. Due to these broad possibilities, many different spinel materials can be synthesised. Indeed, spinels have found wide use in Li-ion batteries as electrodes [2], supercapacitor electrodes [3], thermal barrier coating material [4], as well as in other devices [5–7]. Depending on the chemical composition as well as on the preparation method/thermal history, spinels can be characterised by a broad range of electrical transport properties. It was reported that the electronic conductivity of a spinel occurs mainly by electron hopping between octahedral sites [8,9], and the cation arrangement can depend on the thermal history of the sample.

Manganese-copper-based spinels are interesting materials that have been studied for range of important applications [10–13]. The abundance and low toxicity of Mn and Cu makes the material of interest, especially as a possible replacement of Mn-Co-based spinels, where the mining issues and toxicity of cobalt are problematic. Mn-Cu spinels are already recognised as a potential catalyst for the steam reforming of methanol [14], as a ceramic film for spectrally selective solar-derived applications [15], and also as a protective coating on the interconnects in solid oxide fuel cells [16].

The phase diagram of Mn-Cu-O shows that a pure spinel phase forms only in a relatively narrow compositional and temperature window [17,18]. For this reason, most studied compositions have focused on Mn_2CuO_4 or a slightly modified $Mn_{1.7}Cu_{1.3}O_4$ [19–21]. A increased Cu content shifts the compositions towards a mixture of spinel and CuO, whereas a decreased Cu content, towards a mixture of manganese oxide and spinel.

Petric and Ling investigated the electrical conductivity of $Mn_{1.7}Cu_{1.3}O_4$, which achieved a very high value of 225 S/cm at 750 °C [22]. This is much higher than the electrical conductivity reported for the widely used $MnCo_2O_4$ spinel (~60 S cm^{-1} at 800 °C). Since this work, interest in Mn-Cu spinels has increased. They have been tested as a protective coating for steel interconnects, and as a contacting mesh element in high temperature fuel cells [23–26].

Partial substitution of one of the cations is a well-known way to improve the properties of spinel-based ceramics. This approach has been extensively used to tailor the properties of $MnCo_2O_4$ spinels. Partial substitution of Co by either Fe or Cu has been reported to influence the electrical conductivity and thermal expansion [27–29]. Talic et al. showed that the addition of iron ($MnCo_{1.5}Fe_{0.5}O_4$) decreased the electrical conductivity and the thermal expansion coefficient, whereas the addition of Cu ($MnCo_{1.5}Cu_{0.5}O_4$) resulted in higher electrical conductivity and a higher thermal expansion coefficient [30]. Other studies considered the effect of the addition of Fe/Cu on high temperature corrosion and chromium evaporation of steel interconnects [31–34].

The effects of elemental substitutions in Mn-Cu-based spinels have been studied to a much lesser extent. Bhandage et al. have studied a $Cu_xCd_{1-x}Mn_2O_4$ system [11]. For x = 1, pure cubic phase spinel was obtained, whereas for a composition with x < 0.5, a tetragonal phase was found. The same author also studied the $Ni_xCu_{1-x}Mn_2O_4$ system [12]. Ni substitution in the Mn-Cu spinel was considered as a protective coating and for its effect on high-temperature corrosion protection by Joshi and Petric [35]. Ni stabilised the cubic spinel phase and resulted in a small decrease of electrical conductivity.

A number of synthesis methods have been used for the preparation of different spinel powders, including modified sol-gel [36,37], EDTA gel [38], the glycine nitrate process [39], spray pyrolysis [28,30], co-precipitation [40], and solid state [41,42]. Among the reported methods, the sol-gel-derived routes seem to offer the advantage of cation mixing at the atomic level leading to high homogeneity and formation of small particle sizes [43].

In the present investigation, the $Mn_{1.7}Cu_{1.3}O_4$ spinel was used as the starting material, and its derivatives with partial substitution of Cu by Fe were studied. The influence of iron substitution on its properties, related to SOFC interconnect protection, namely sintering behaviour, crystal structure, and electrical conductivity was evaluated.

2. Experimental

2.1. Powder preparation

Spinel powders with the general formula $Mn_{1.7}Cu_{1.3-x}Fe_xO_4$, where x=0, 0.1, 0.3, and 0.5, were synthesised by a modified Pechini method [44]. Throughout the paper, the powders and sample compositions are abbreviated according to Table 1. The starting substrates used in the syntheses were hydrated nitrate salts of metals: manganese (II) nitrate ($Mn(NO_3)_2{\cdot}4H_2O$, Sigma Aldrich, ≥97%), copper (II) nitrate ($Cu(NO_3)_2{\cdot}H_2O$, Sigma Aldrich, 99.999%), and iron (III) nitrate ($Fe(NO_3)_3{\cdot}9H_2O$, Sigma Aldrich, 99.999%). Water solutions of dissolved nitrates with known concentrations (pre-standardised thermogravimetrically) were mixed together in the proper molar ratio corresponding to the intended nominal composition of the spinel powders. The water solutions containing all of the desired cations were heated under constant stirring to 80 °C (controlled using an insertion probe) on a magnetic stirring hot plate. Citric acid ($C_6H_8O_7$, Sigma Aldrich, 99%), and EDTA ($[CH_2N(CH_2CO_2H)_2]_2$, Sigma Aldrich, 99%) were added to the solution under stirring as chelating agents in the molar ratio 2:1:1-TMI (total molar ions). To control the pH at the desired level of 8, diluted ammonia (25% aqueous solution) was added dropwise. To start the transesterification process, ethylene glycol ($C_2H_6O_2$, Sigma Aldrich, 98%) was added under continuous stirring, in the amount to obtain a ratio of 1 mol of polyalcohol to 1 mol of metal cations. The liquid precursor was then held at 80 °C until a dense gel-like structure was obtained. It was further dried at 130 °C for 4 h. The resulting material was placed in a muffle furnace and heated to 400 °C for 2 h. The obtained powder was ground in an agate mortar and further calcined at 900 °C for 2 h. In the end, the powders were again ground in the agate mortar and used for further studies.

2.2. Pellet preparation

Ceramic pellets were prepared from the synthesised powders by uniaxial pressing in a hydraulic press (Carver, USA). The powders were compacted using 54 MPa pressure. The obtained disk-shaped green bodies had a diameter of ~16 mm and a thickness of 1.5–2 mm. The pressed pellets were sintered at three different temperatures: 900 °C, 1000 °C, and 1100 °C in air. Heating and cooling rates of 3.6 °C min^{-1} were used with a dwell time of 2 h. The dimensions of the sintered pellets were measured (using a Mitutoyo micro-caliper) to calculate the linear shrinkage. The porosity of the sintered pellets was determined from analyses of SEM images of polished cross-sections. For each sample, ten images were taken at the same magnification, and these images were analysed using the ImageJ software [44].

2.3. Materials characterisation

The x-ray diffraction (XRD) technique was used to determine the phase composition and the crystal structure of the fabricated powders. The measurements of the synthesised powders were conducted at room temperature using a Bruker D2 Phaser 2nd generation diffractometer with CuKα radiation ($\lambda = 1.5404$ Å) and XE-T detectors. Data were collected from $2\theta = 10°$ to $90°$ with a step size of 0.01° and acounting time of 0.2 sec for each step. The results were processed by means of LeBail refinement using the Bruker Topas software.

High temperature X-ray powder diffraction data were collected on a Philips X'Pert Pro diffractometer, fitted with an X'Celerator detector, using Ni filtered Cu-Ka radiation ($l_1 = 1.54056$ Å and $l_2 = 1.54439$ Å). Elevated temperature measurements were performed using an Anton-Paar HTK 1200 high temperature camera. Data were collected in flat plate θ/θ geometry on a Pt-coated sample holder. Calibration was carried out with an external LaB_6 standard. Diffraction patterns were acquired at room temperature and at 50 °C intervals from 50 °C to 850 °C in air. Data at room temperature and at 850 °C were collected over the range 5–105° 2θ, in steps of 0.033°, with an effective scan time of 120 s per step. Shorter scans were performed for intermediate temperatures with an effective scan time of 40 s per step.

Thermogravimetric analysis (TGA) of the studied oxides was performed using a Netzsch TG 209 F3 Tarsus thermobalance. The measurements were carried out both in air and argon atmospheres. The mass change was observed up to 900 °C with a heating and cooling rate of 3 °C min^{-1}.

Dilatometric studies of the sintering and thermal expansion were carried out using a Netzsch DIL402 dilatometer. Measurements were performed in a synthetic air atmosphere with a heating rate of 5 °C min^{-1}, with a 15 minutes isothermal step at 1100 °C and a cooling rate of 3 °C min^{-1}.

The phase diagram of $Cu\text{-}O_2$ was calculated using the FACTSAGE software and databases [45].

Scanning electron microscopy (SEM) investigation of the powders and pellet cross sections were carried out on a Phenom XL (Thermo Fisher Scientific) desktop SEM equipped with an integrated energy dispersive X-ray (EDX) microanalyser. For preparation of the pellet cross sections, samples were mounted in epoxy (EpoFix, Struers) and then polished on a semi-automatic Struers Tergamin-20 machine down to a 1 µm finish.

The electrical conductivity of the pellets was estimated by employing the van der Pauw method [46]. The samples were heated to 900 °C and measured down to 200 °C with decrements of 50 °C in air. The activation energy, E_a, was calculated using the formula, derived from the Arrhenius equation:

$$ln\sigma T = \frac{-E_a}{k} \times \frac{1}{T} + ln\sigma_0, \qquad \text{(Eq.1)}$$

where σ — electrical conductivity, T — temperature, σ_0— pre-exponential factor, E_a— activation energy, and k — Boltzmann's constant.

Electrical conductivity data were corrected for sample porosity with using the Brueggemann asymmetric model, according to the following formula [47]:

$$\sigma = \sigma_m \cdot \frac{1}{(1-p)^{\frac{3}{2}}}$$

Where Ϭ is the corrected conductivity, $Ϭ_m$ is the measurement conductivity and p is sample porosity.

3. Results and discussion

3.1. Chemical, microstructural and sintering characterisation of the powders

Chemical and morphological analysis of the powders

After the milling process, the powders were characterised for their elemental compositions, morphologies, and phase structures. EDX analyses were performed on the powders to determine the atomic compositions of the calcined powders. The results of the analyses are presented in Table 1 (with the accuracy of EDX method +/- 1%). The calculated Mn/(Mn+Fe) and Fe/(Fe+Cu) cation ratios correspond well to the expected stoichiometries.

Table 1. Chemical composition of powders determined by means of EDX and sample's names used in this paper.

Desired composition	Sample name	Metal ratio			Mn / Cu+Fe	Fe / Fe+Cu	Corresponding spinel composition
		Mn	Cu	Fe			
$Mn_{1.7}Cu_{1.3}O_4$	0Fe	0.56	0.44	-	1.27	-	$Mn_{1.68}Cu_{1.32}O_4$
$Mn_{1.7}Cu_{1.2}Fe_{0.1}O_4$	01Fe	0.59	0.38	0.03	1.43	0.07	$Mn_{1.73}Cu_{1.15}Fe_{0.12}O_4$
$Mn_{1.7}Cu_1Fe_{0.3}O_4$	03Fe	0.56	0.34	0.10	1.27	0.23	$Mn_{1.69}Cu_{0.99}Fe_{0.32}O_4$
$Mn_{1.7}Cu_{0.8}Fe_{0.5}O_4$	05Fe	0.57	0.25	0.18	1.32	0.42	$Mn_{1.69}Cu_{0.76}Fe_{0.54}O_4$

Figure 1 presents a representative SEM micrograph of the 05Fe powder after calcination at 900 °C and after milling in an agate mortar. All of the powders were composed of micron-sized particles (~1–3 µm) without the presence of larger agglomerates. No influence of iron substitution on the particle size could be observed.

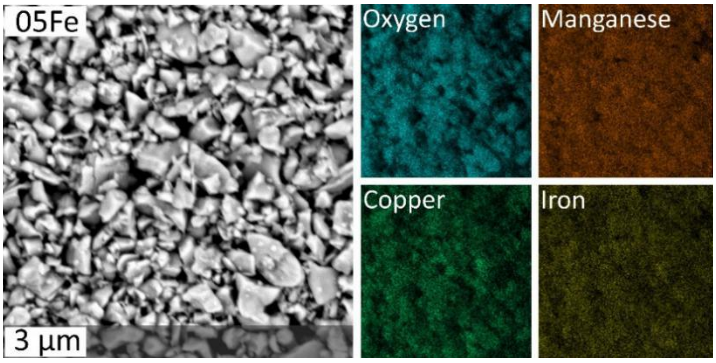

Figure 1. Scanning electron microscopy image and energy dispersive elemental analysis of the 05Fe ($Mn_{1.7}Cu_{0.8}Fe_{0.5}O_4$) powder.

Room-temperature XRD analysis of the powders

The room temperature XRD patterns of the calcined powders are shown in Figure 2a (full measured range) and 2b (enlargement of the main peak region). The non-substituted 0Fe powder revealed the existence of a cubic spinel phase (space group Fd-3m, ICDD card #35-1030) with a possible very small addition of CuO (estimated to <3 vol.%, monoclinic structure, space group c2/c, #45-937). The observation of these two phases is in agreement with the Cu-Mn-O phase diagram, where single-phase cubic might decompose at low temperatures to spinel + MnO_2, or to MnO_2 + CuO [17,18,20]. A quite similar structure was observed for the 01Fe powder. Only the cubic spinel and a small amount of another phase could be seen. It must be noted that the peaks ascribed to CuO might also have been caused by the cubic (#35-1030) or tetragonal ($CuMn_2O_4$, #71-1141) spinel phase. Due to overlapping peaks and small relative intensity, the exact determination of the minority phase is not possible. The presence of minor phase impurities in $Cu_{1.3}Mn_{1.7}O_4$ is known in the literature, for example, Bobruk et al. observed the same level of CuO-attributed peaks in this material, synthesised by EDTA-gel processes and calcined at 700 °C [38]. The introduction of iron shifted the ~36° peak position towards the higher 2θ angle, evidencing contraction of the unit cell, compliant with a smaller size of the Fe cations than Cu cations.

The increase in Fe-content resulted in the formation of a new phase, which can be attributed to a tetragonal spinel structure (space group: I41/amd:2) [48]. No indications of iron oxides could be found in the spectra either. For the 03Fe powder, the cubic spinel peak had the highest intensity, whereas for the 05Fe powder, the tetragonal phase dominated.

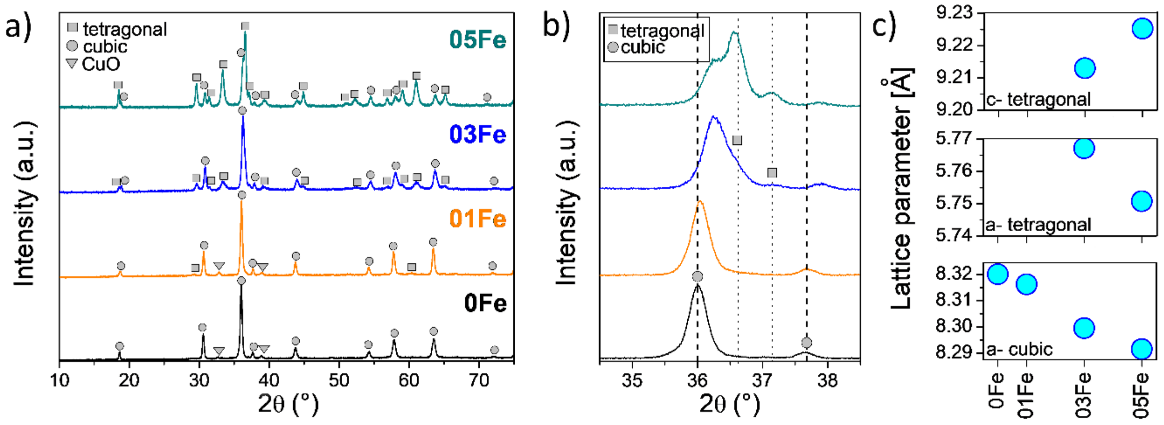

Figure 2. X-ray diffraction patterns of powders synthesised via the EDTA-CA gel process after calcination at 900 °C (a, b). Lattice parameters (at room temperature), determined by structure fitting of XRD patterns for spinel powders calcined at 900 °C (c).

The lattice parameters determined by structure fitting of the cubic Fd-3m space group and tetragonal I41/amd:2 are plotted in Figure 2c and summarised in Table 2. The cubic spinel phase changed the unit cell size (“a” parameter) linearly with the substitution of copper with iron. For the tetragonal phase, the unit cell size showed a more complex behaviour. The “a” parameter decreased its value, whereas the “c” parameter increased.

The formation of the tetragonal phase in the Mn-Cu spinel can be explained by the Jahn-Teller effect, i.e. the elongation of the octahedral in the “c” direction [49]. This was caused by the presence of octahedrally coordinated Mn^{3+} cations (or possibly also Cu^{2+}) [49,50]. Mn-Cu spinels are interesting as materials which contain two Jahn-Teller ions: Mn^{3+} and Cu^{2+}[18]. Baffier and Huber argued that for the formation of a tetragonal structure, the relative concentration of Mn^{3+} ions needs to be high, i.e. >50% of the sites [10,51]. The addition of iron thus resulted in the formation of Mn^{3+} in octahedral positions (or Cu^{2+}), which allowed for the incorporation of the copper cations into the spinel structure. The elongation of the unit cell in one direction (“c”) was followed by contraction of the unit cell in the “a” direction.

The effect of cation substitution in the spinel structure cannot be resolved simply due to the complexity of the structure, i.e. the presence of tetrahedral and octahedral positions and multiple possible valence states of the cations. Due to the multitude of the possible arrangements and cation sizes, it is hard to determine where the newly introduced cations are situated. As evidenced by XRD, partial substitution of Cu by Fe led to the decrease of the lattice parameter “a”, as shown in Table 2. In general, iron cations are smaller than copper cations, so a decrease of the cell-size parameter can be expected. Manganese has a strong tendency to occupy the octahedral position. Due to the high Cu content in the $Mn_{1.7}Cu_{1.3}O_4$ spinel, some Cu should also occupy the octahedral position, with the remaining Cu in the tetrahedral position. The situation is also complicated by the fact that, at room temperature, the compositions rich in iron (03Fe and 05Fe) are not single phase — they form a mixed cubic-tetragonal oxide, where the cations' distributions will be further confounded. Therefore, in this paper, we do not propose any specific cationic distribution, as it is far too complex and uncertain in our view. A summary of the reported possible cation distributions in the Mn-Cu spinels can be found in [18].

Table 2. Lattice parameters for cubic and tetragonal phases determined by Le Bail refinement (at room temperature).

Powder	Phase:	Cubic	Tetragonal			
		a_C [Å]	a_T [Å]	$a_{T'}$ [Å]	c_T [Å]	c_T / $a_{T'}$
0Fe	C	8.3201(5)				
01Fe	C	8.3162(1)				
03Fe	C+T	8.2995(4)	5.7672(2)	8.13175	9.2133(2)	1.13
05Fe	C+T	8.2915(6)	5.7508(3)	8.1086	9.2253(4)	1.14

High-temperature XRD analysis of the powders

In order to follow the development of the phase-composition of the materials vs. temperature, in-situ high-temperature XRD analyses were performed. The results are presented in Figure 3a–d.

For the 0Fe and 01Fe, the cubic phase did not change upon heating. Above 500 °C, the occurrence of a new phase could be noticed for both powders. It is ascribed to CuO, which is in line with the phase diagram [17] and discussion by Martin and Petric [20]. According to the phase diagram, the pure spinel phase was stable in only a quite narrow temperature window (roughly between 500 °C and 600 °C). For the 03Fe and 05Fe powders, where the cubic and tetragonal phases co-existed at room temperature, transformation into a single cubic phase was observed at >400 °C. In the case of the 05Fe powder, the tetragonal phase remained stable at 400 °C, whereas for the 03Fe powder, it seemed to disappear at 400 °C. CuO also seemed to form in the 03Fe powder, whereas it was not detected in the 05Fe powder. The addition of Fe stabilised the spinel phase, which was a mixture of tetragonal-cubic below 500 °C and transformed into a fully cubic spinel at >500 °C.

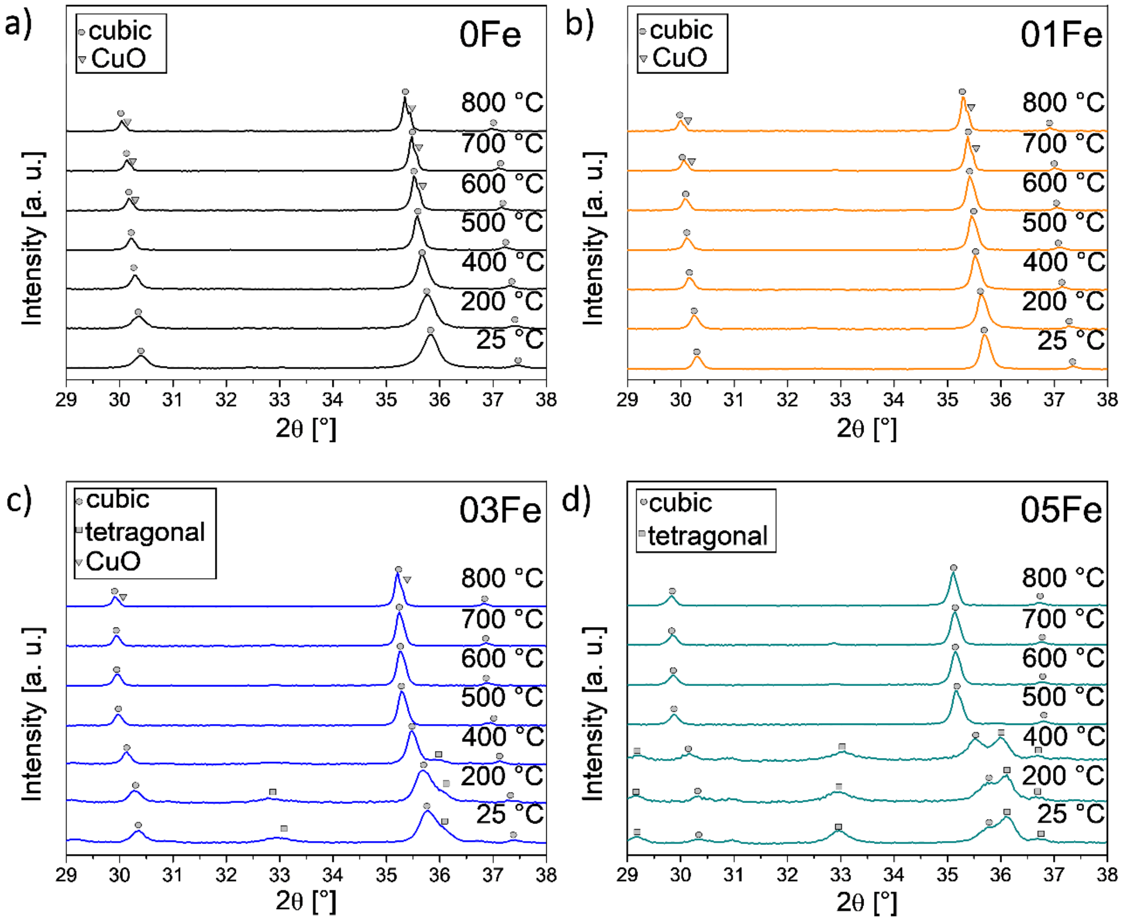

Figure 3. High-temperature XRD (25–800 °C in air) patterns for the powders: 0Fe(a), 01Fe (b), 03Fe (c), and 05Fe (d).

Dilatometry study

Following the phase characterisation was the determination of the sintering properties of the prepared compounds. A dilatometry study was performed in order to determine the shrinkage profiles of the compacted powders (up to 1100 °C) and thermal expansion coefficient (TEC) values. In addition to the measurements performed in the dilatometer, the diameters of the pellets were analysed before and after ex-situ sintering in a furnace at different temperatures (900 °C, 1000 °C, and 1100 °C). The dilatometry curves and values of relative shrinkage for the pellets are presented in Figure 4a–c.

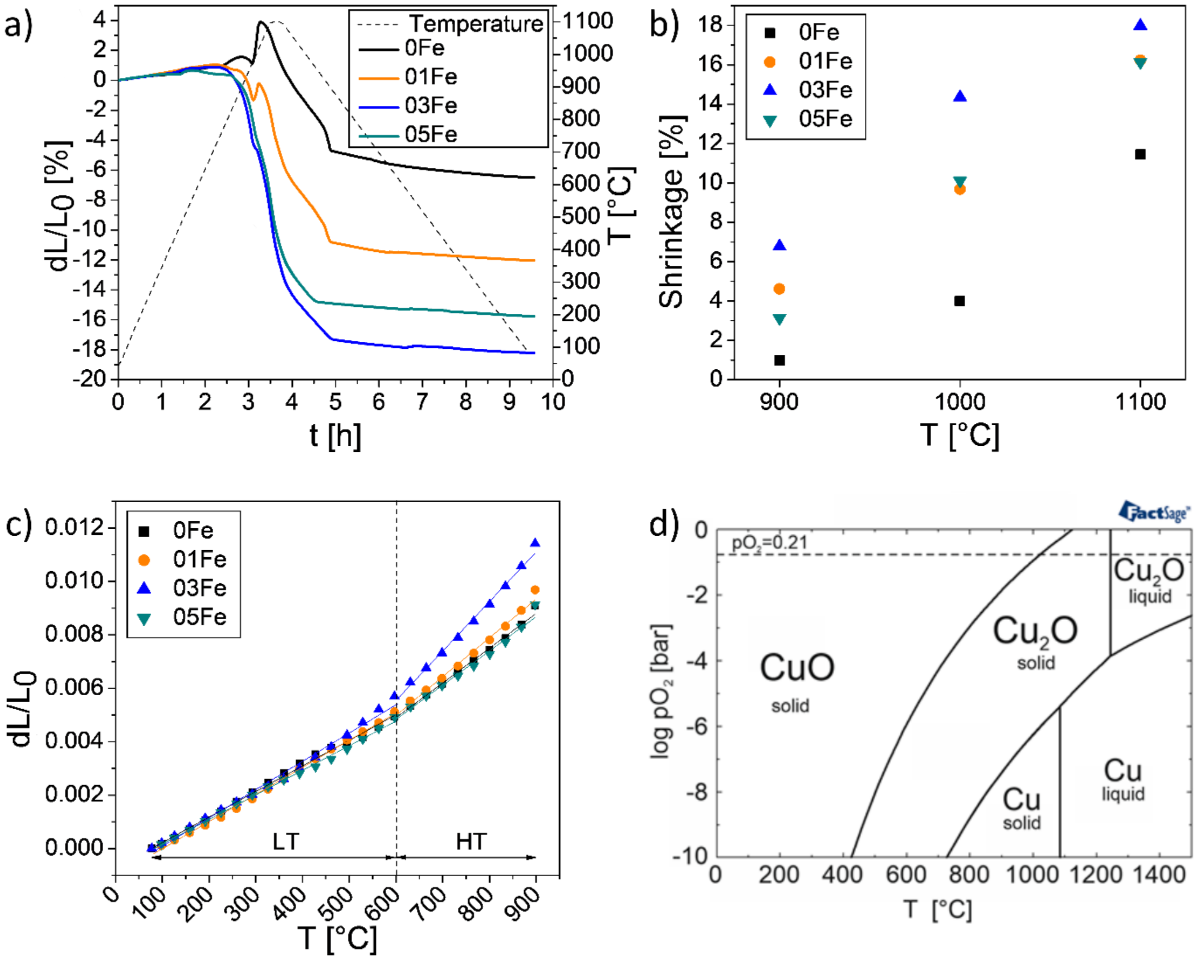

Figure 4. Dilatometry results (in air) for sintering of the powders (a), relative shrinkage of the pellets measured after sintering the green bodies at 900 °C, 1000 °C, 1100 °C (b), thermal expansion of the spinel pellets, pre-sintered at 1100°C (cooling cycle from 900 °C in air) (c), and phase diagram of Cu-O$_2$ showing the phase change of CuO to Cu$_2$O (d).

The sintering behaviour of the materials differed considerably (Figure 4a). Intense expansion was visible, especially for the non-iron-doped spinel, upon heating at ~1000 °C. The sample expanded by ~4% within a few minutes, and then the sintering began. Quite similar behaviour was visible for the 01Fe powder, but to a smaller extent, potentially due to the earlier onset of sintering, as the sample started to sinter at ~850–900 °C. The observed behaviour can be attributed to reduction of the CuO phase, which formed upon heating of the spinel, as described in the HT-XRD discussion (see Figure 3). CuO phase reduced into the Cu$_2$O phase in this temperature range (~1000 °C), well in line with the Cu-O-temp phase diagram presented in Figure 4d and the literature [52,53]. For the 03Fe and 05Fe materials, where less or no CuO was detected in the XRD spectra, no such peaks in the dilatometry curves were visible. These powders started to sinter at ~800 °C and followed a regular sintering pattern. The largest shrinkage was observed for the 03Fe sample (~18%), followed by the 05Fe sample (~16%). The continuous dilatometry results were confirmed by the ex-situ pellet diameter measurements: the smallest shrinkage was obtained for the 0Fe samples, followed by 01Fe and 05Fe, while the largest shrinkage was obtained for the 03Fe sample. The shrinkage values (Figure 4 b) demonstrate that iron doping sufficiently enhanced the sinterability of the studied materials, however fabrication of the ceramics with low porosity in air required temperatures above 1000 °C.

Thermal expansion coefficients were determined using data collected during cooling of the samples from 900 °C (samples were sintered in air at 1100 °C). As the curves were not linear in the 50–900 °C temperature range, the analysis region was divided into high temperature (600–900 °C) and low temperature (50–600 °C) intervals. The calculated TEC values are presented in Table 5. For the high temperature domain, thermal expansion demonstrated a complex effect of the iron doping, with an apparent maxima for the 03Fe ceramic. In the low temperature region, all of the sintered samples had a TEC of 9.2–10.6 $x10^{-6}$ K^{-1}. In general, iron substitution did not have a strong influence on the thermal expansion.

Thermogravimetric analysis

In addition to dilatometry, thermogravimetric analyses were performed. TGA revealed that $Mn_{1.7}Cu_{1.3-x}Fe_xO_4$ complex oxides demonstrated sufficient activity in oxygen exchange with the environment (Figure 5a–e). For the 0Fe, upon heating from room temperature to 900 °C, the sample initially gained weight (~0.05%), which started at ~400 °C, then at around 700 °C it started losing weight (Figure 5b first cycle of heating, and Figure 5d second cycle of heating). The sample with no iron was the only one to show no notable weight increase upon heating. The addition of iron suppressed the weight loss effect. For the 01Fe and 03Fe, the weight loss started at ~700 °C and had a much smaller extent than the weight loss of the 0Fe. For the 0Fe powder, at isothermal hold at 900 °C, the weight change had not stabilised after 2 hours, which indicates relatively slow equilibration. The 01Fe and 03Fe powders seemed to stabilise their weight change faster (Figure 5e). For the 05Fe sample, neither weight gain nor weight loss was found. The 05Fe powder was practically inert in air, which supports the expectation of good stability in oxidising atmospheres at high temperatures. When cooling (Figure 5d), the mass change process was reversible, which confirms that this phenomenon is related to the stability of the tested materials and the oxidising atmosphere. The weight loss can be explained as a result of the formation of a CuO phase: the O/Cu ratio was lower in the CuO than in the spinel, therefore segregation of the CuO resulted in net loss of weight. At high temperature (~900 °C) the reduction of CuO to Cu_2O is also possible, visible in Figures 5c and 5e, in-line with the phase diagram presented in

Figure 4d. The weight loss trend corresponds well with the amount of possible CuO formation: for the 05Fe, where no CuO was detected upon heating, there was no weight loss, and the sample was stable upon heating, while for the 0Fe, it was very prominent. One can note that the behaviour of the 03Fe demands presence of traces of CuO, confirming the XRD observation. This might explain the behaviour of the dilatometric curve for this material as well as its electric conductivity: the amount of iron in the 03Fe was not sufficient to keep the Cu in the cubic phase, so CuO particles grew during heating, which led to the rise of the TEC and changes in electrical conductivity.

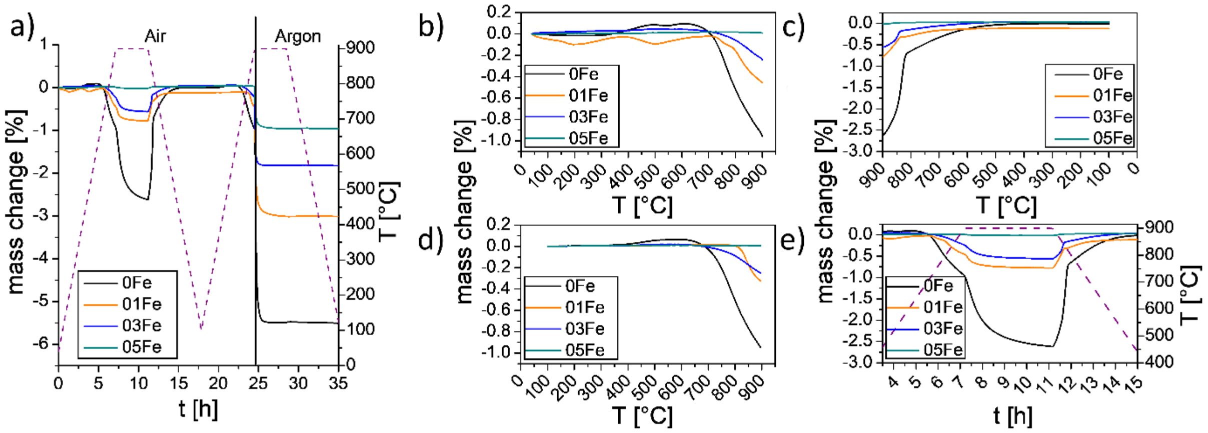

Figure 5. Mass change of the $Mn_{1.7}Cu_{1.3-x}Fe_xO_4$ powders in air as a function of time (a), first heating ramp (b), first cooling ramp (c), second heating ramp (d), and isothermal hold after first heating ramp (e).

3.2. Electrical conductivity characterisation of the spinels

The electrical properties of the materials were analysed by studying the DC electrical transport properties of the sintered pellets in air in the temperature range 900–200 °C. To evaluate the effects of porosity and thermal treatment in general, pellets prepared from the 0Fe, 01Fe, 03Fe and 05Fe powders were sintered at either 900 °C, 1000 °C, or 1100 °C in air. The results of the measurements are presented in Figure 6a–e.

The behaviour of the samples depended on the iron substitution level, as summarised in Figure 6a. For the sample without iron (0Fe, Figure 6b) and with low iron content (01Fe, Figure 6c), the electrical behaviour was notably different than for the samples with higher iron content (03Fe and 05Fe, Figures 6d and 6e, respectively). For the 0Fe and 01Fe, the maximum electrical conductivity was reached at ~650 °C. The maximum conductivity value was quite similar, reaching ~180 S cm^{-1}, which can be considered very high (the small difference between the samples is within the experimental error margin of ±5%). Below the maximum, the conductivity was thermally activated, whereas above the maximum, the conductivity decreased with temperature increase. The point (temperature) of conductivity maximum coincided with the point where the spinels started losing weight. This was thus also connected to the formation of the CuO phase. Similar effects have been described by Martin and Petric [20]. They also measured thermopower and determined that the majority of carriers are electron holes (p-type conductivity).

For the samples with higher iron content, i.e. the 03Fe and 05Fe, the conductivity exhibited a clear transition point, where the levels of electrical conductivity step-changed, and for which different activation energies were found. The transition temperature was ~400 °C and was caused by a phase transition from mixed cubic-tetragonal phases to a pure cubic spinel phase (at high temperatures). Interestingly, the 03Fe and 05Fe pellets sintered at 1100 °C did not show such a phase transition; only a slight change of slope of the conductivity curve.

Samples with higher iron content showed generally lower conductivity values and a regular thermally activated behaviour across the full temperature range. For the 03Fe sample, the conductivity was highest after sintering at 1000 °C; sintering at a higher temperature reduced the conductivity. All of the other compositions showed an increase of electrical conductivity upon increasing the sintering temperature. The 03Fe sample showed a conductivity value of ~120 S cm^{-1}, whereas the 05Fe sample had a conductivity of ~30 S cm^{-1} at 650 °C. As shown in Figure 6, due to the thermal activation across the full temperature range, the electrical conductivity of the 03Fe sample became highest for temperatures above 800 °C. Although the electrical conductivity values clearly depended on the iron content, they can all be considered relatively high. Based on the results, it can be stated that the electrical conductivity of the tetragonal phase (the low temperature phase) is greatly reduced in comparison to the conductivity of the cubic phase.

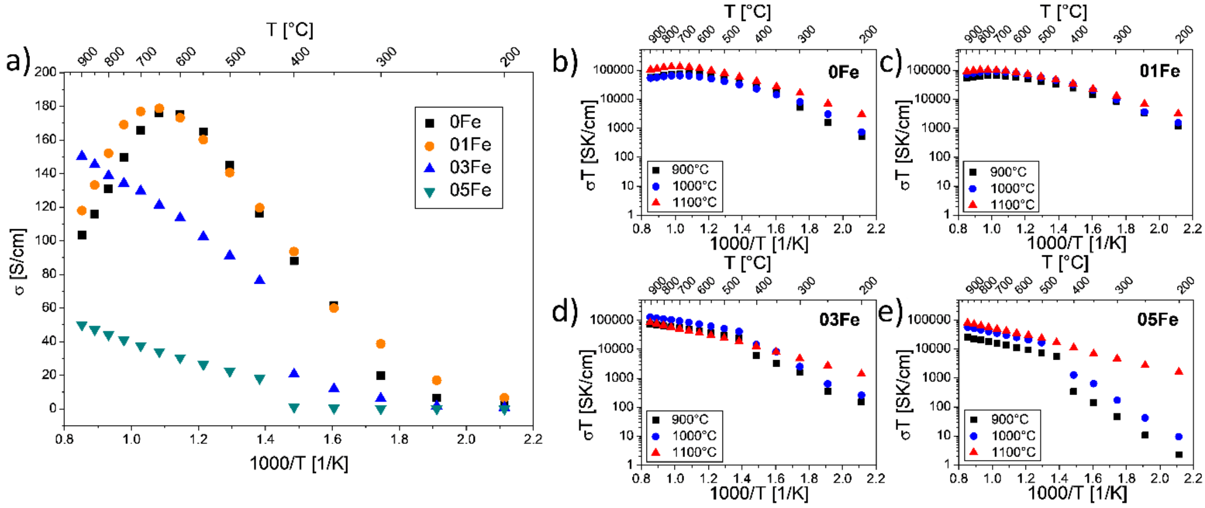

Figure 6. Electrical conductivity plot of the 0Fe, 01Fe, 03Fe and 05Fe samples measured on pellets sintered at 900 °C (a)- results were corrected for sample porosity. Arrhenius plots of electrical

conductivity as a function of pellet sintering temperatures (900 °C / 1000 °C / 1100 °C). Results were not corrected for sample porosity.

Based on the Arrhenius plots (Figure 6b–e), the activation energies of the electrical conductivity were calculated and are presented in Table 3. Due to the visible change in the slopes, the activation energies were calculated separately for two temperature ranges: 450–650 °C and 200–400 °C. These two ranges have distinctly different value levels. At high temperatures, the activation energies were rather low, with values in the range 0.20–0.30 eV and did not seem to depend on the sintering temperature. At lower temperatures, variation of the activation energies was quite significant. The lowest values were found for the highest sintering temperature of 1100 °C (between 0.26 eV for the 05Fe sample, and 0.37 eV for the 0Fe) and were only slightly higher than the values obtained at high temperatures. For lower sintering temperatures, the activation energies were in the range of 0.4 to 0.7 eV. In general, the obtained values are in agreement with typical reported values for different spinels [29,30,38]. The difference between the low and high temperature values of the activation energy may be connected to different grain and grain boundary contributions to the total electrical conductivity [54].

Table 3. Thermal expansion coefficients of the sintered spinels (from Figure 4c) and activation energy of the electrical conductivity (E_A) fitted according to Eq. 1 for two temperature ranges (200–400 °C and 450–650 °C) for each featured material sintered at three temperatures (from Figure 6b–e).

	Thermal expansion coefficient TEC [x10^{-6} K^{-1}]		Activation energy for the electrical conductivity E_A [eV]					
Temperature range	50 °C-600	600 °C-900°C	200 °C - 400 °C			450 °C- 650 °C		
$T_{sintering}$/ composition	1100 °C		900 °C	1000 °C	1100 °C	900 °C	1000 °C	1100 °C
0Fe	9.57	13.01	0.57	0.47	0.37	0.22	0.22	0.25
01Fe	10.15	14.52	0.41	0.43	0.33	0.20	0.21	0.21
03Fe	10.58	18.57	0.53	0.58	0.31	0.21	0.22	0.25
05Fe	9.19	12.81	0.70	0.69	0.26	0.25	0.25	0.27

3.3. Microstructural properties of sintered materials

In order to characterise the properties of the materials in more detail, XRD and SEM/EDS analyses of the differently sintered pellets were performed. Images of polished cross-sections of all of the samples are presented in Figure 7, with accompanying elemental maps and chemical compositions in the supplementary materials (Figure S1, Table S1). Based on the images, the porosities of the pellets were determined and the values are included in the figure. The samples sintered at 900 °C showed similar, porous microstructures (porosities ~40–47%). For the samples containing iron, the particle sizes seemed to be smaller than for the non-substituted sample, where large well-sintered structures could be found. For samples sintered at 1000 °C the porosities were considerably lower (~20–30%), and a clear difference in the microstructure was obtained for the 0Fe sample. It was characterised by high density and showed the presence of different phases (different shades of grey). The iron-doped samples showed high density and a small amount of secondary phases. For the samples sintered at 1100 °C, the microstructure was quite dense for all samples (porosities 5–20%), and the presence of secondary phases with different chemical compositions were detected for the 0Fe, 01Fe and 03Fe samples in increasing amounts, as can be expected from the XRD data. For the 05Fe sample, no inhomogeneity in the chemical composition was detected by SEM/EDS. XRD analyses of the pellet samples shown in Figure 7 were performed on powders obtained from crushed pellets (XRD spectra are presented in Figure S2). The structural results comply with other data. For a sintering temperature of 900 °C, the phase composition was relatively simple, and pure spinels were obtained (either in cubic, or cubic + tetragonal form) with a minor CuO phase for the 0Fe and 01Fe. Sintering at temperatures of 1000 °C and above resulted in the formation of new phases. By analysing the phase diagrams,it can be seen thatabove 900 °C, the formation of a $CuMnO_2$ phase started[20], with the formation of a $Cu_5Mn_4O_9$ phase above 975 °C [18]. Generally, based on the results and the published phase diagrams, the structure of the Mn-Cu spinels is retained up to <1000 °C.

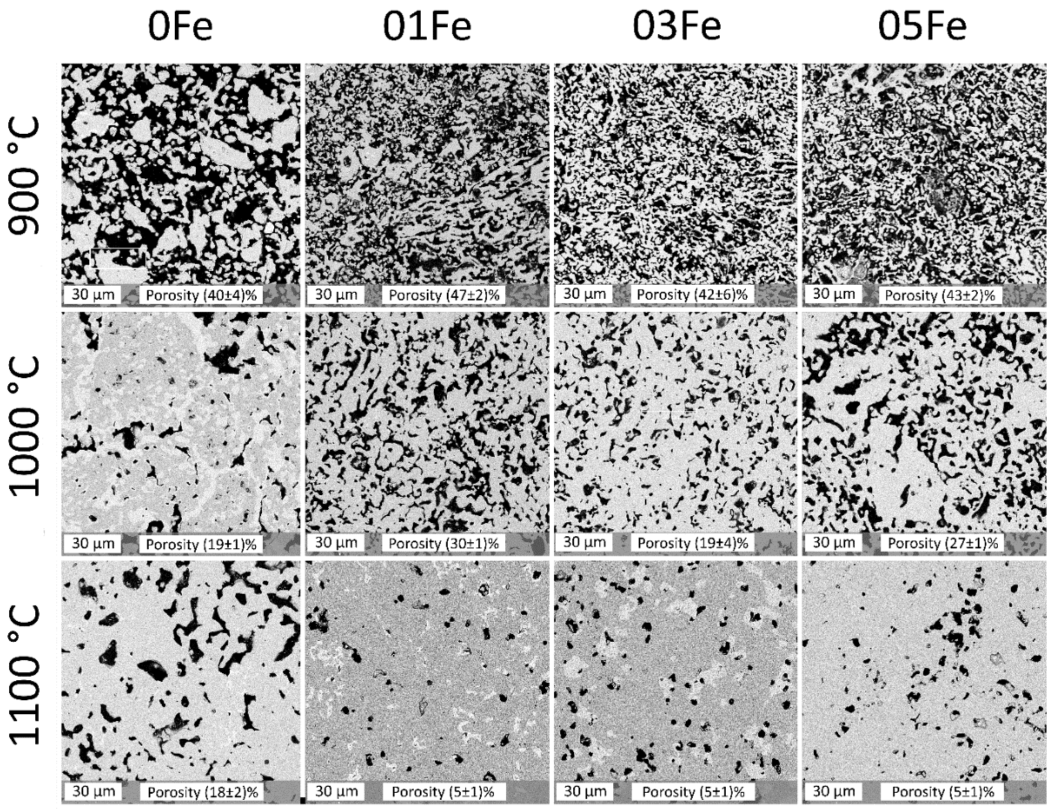

Figure 7. SEM cross-section images of pellets sintered at different temperatures.

3.4. General discussion

Based on the obtained results, the effect of iron substitution in the Mn-Cu oxide spinel can be discussed. In general, Mn-Cu-based spinels are complex materials, which exhibit quite narrow single-phase regions in phase diagrams. By using a specific Mn:Cu ratio (e.g. 1.7:1.3), it is possible to obtain a pure cubic phase at room temperature, and up to ~600 °C, where CuO starts forming. By adding iron, the stability of the spinel lattice is extended. At room temperature, the 05Fe spinel is a mixture of cubic and tetragonal phases, that upon heating to >400 °C form a single cubic phase, which does not show decomposition into CuO upon further heating. Stabilisation of the spinel phase is important, as for the CuO-containing compositions, reduction to Cu_2O happens at high temperatures. This reduction induces volume changes and can have a negative impact on the material's stability. Due to the precipitation of CuO, the electrical conductivities of the spinels differ. Precipitation of CuO results in lowering of the electrical conductivity, evidenced by a maxima in the conductivity curves, which indicates an important role of copper in the electrical conductivity. By adding Fe, CuO formation is suppressed, and the electrical conductivity follows a pattern expected for a thermally activated semiconductor with visible phase transition to a fully cubic structure.

3.5. Possible application of the iron-substituted Mn-Cu spinel in solid oxide cells

Though not specifically discussed above, iron-substituted spinels are being developed as potential protective coating materials for steel interconnects for high-temperature solid oxide cells. Currently, the state of the art is the $MnCo_2O_4$ spinel, which shows good protective behaviour, but contains harmful and nonsustainably mined cobalt. Also, there is a strong need for cobalt in the rapidly developing Li-ion market. The results obtained in this work point to the potential applicability of the newly developed materials as protective coatings:

- Values of the TEC for the spinels might be considered to becompatible with Crofer 22 APU [55] or 441-type ferritic steel [56], which are used for the fabrication of SOFC interconnects;
- Electrical conductivity of the spinels is sufficiently high at operating temperatures (> 10 S cm^{-1} at 700–800 °C) [57];
- Iron substitution improves the sinterability of the spinels. Typically, the coatings are sintered via a reduction and subsequent reoxidation process. Lowering the sintering temperature can help with decreasing the reoxidation temperature from 900 °C [58] to 800°C or time used in coating densification process with the comparison of sintering condition for state of the art Mn_2CoO_4.
- Iron-substituted spinels show thermochemical stability in oxidising conditions at high temperatures.

To prove the suitability of the materials for protective coatings for steel interconnects, further tests need to be carried out: specifically, issues including optimization of the coating process, sintering conditions, adhesion test, reactivity with Cr, area-specific resistant measurements and long-term corrosion properties (e.g. oxide scale growth kinetics) need to be evaluated. From a materials perspective, however, Fe-modified Mn-Cu spinels seem to have suitable physico-chemical properties for a successful protective coating.

4. Conclusions

In this work, Fe substituted $Mn_{1.7}Cu_{1.3-x}Fe_xO_4$ spinel-based ceramics (x=0, 0.1, 0.3, 0.5) were synthesised and characterised. Adding small amount of Fe (x = 0.1) does not alter the properties considerably. On the other hand, adding more iron (x = 0.3 or 0.5) results in the formation of the tetragonal spinel due to Jahn-Teller distortion of the octahedra, the change in electrical conductivity properties, and improved stability of the spinel phase (less or no CuO formation). The sinter-activity of the powders is increased with the addition of iron, whereas the thermal expansion remains similar. Iron stabilised the spinel phase, thus no CuO is reduced at high temperatures, and thermal stability of the spinels is improved. The addition of iron results in lowered electrical conductivity. For the 0Fe and 01Fe a maxima in electrical conductivity values were found and correlated to the formation of the CuO phase. For the 03Fe and 05Fe, no maxima were found, and the samples follow a linear, thermally activated behaviour.

To conclude, the results show that partial substitution of Cu by Fe in the Mn-Cu spinel leads to suppression of the formation of CuO_x at high temperatures, which improves the thermomechanical properties and sinterability of the ceramics. The concomitant trade-off in electrical properties leaves absolute values of conductivity on the level desirable for SOFC/SOEC applications.

Acknowledgments

This project is supported by National Science Centre (NCN) Harmonia 9 project number UMO-2017/26/M/ST8/00438: “Quest for novel materials for solid oxide cell interconnect coatings”. Funding of WETI PG is also gratefully acknowledged.

References

[1] Q. Zhao, Z. Yan, C. Chen, J. Chen, Spinels: Controlled Preparation, Oxygen Reduction/Evolution Reaction Application, and Beyond, Chem. Rev. (2017) acs.chemrev.7b00051. https://doi.org/10.1021/acs.chemrev.7b00051.

[2] K.M. Shaju, P.G. Bruce, Nano-LiNi0.5Mn1.5O4 spinel: a high power electrode for Li-ion batteries, Dalt. Trans. 0 (2008) 5471. https://doi.org/10.1039/b806662k.

[3] Y. Zhu, X. Ji, Z. Wu, W. Song, H. Hou, Z. Wu, X. He, Q. Chen, C.E. Banks, Spinel NiCo2O4 for use as a high-performance supercapacitor electrode material: Understanding of its electrochemical properties, J. Power Sources. 267 (2014) 888–900. https://doi.org/10.1016/J.JPOWSOUR.2014.05.134.

[4] S. Chen, X. Zhou, W. Song, J. Sun, H. Zhang, J. Jiang, L. Deng, S. Dong, X. Cao, Mg 2 SiO 4 as a novel thermal barrier coating material for gas turbine applications, J. Eur. Ceram. Soc. 39 (2019) 2397–2408. https://doi.org/10.1016/j.jeurceramsoc.2019.02.016.

[5] M. Zawadzki, W. Walerczyk, F.E. López-Suárez, M.J. Illán-Gómez, A. Bueno-López, CoAl2O4 spinel catalyst for soot combustion with NOx/O2, Catal. Commun. 12 (2011) 1238–1241. https://doi.org/10.1016/J.CATCOM.2011.04.021.

[6] S. Takahashi, H. Ogawa, A. Kan, Electronic states and cation distributions of MgAl2O4 and Mg0.4Al2.4O4 microwave dielectric ceramics, J. Eur. Ceram. Soc. 38 (2018) 593–598. https://doi.org/10.1016/j.jeurceramsoc.2017.08.022.

[7] H. Jia, W. Zhou, H. Nan, J. Dong, Y. Qing, F. Luo, D. Zhu, Enhanced high temperature dielectric polarization of barium titanate/magnesium aluminum spinel composites and their potential in microwave absorption, J. Eur. Ceram. Soc. 40 (2020) 728–734. https://doi.org/10.1016/j.jeurceramsoc.2019.11.003.

[8] Y. Liu, J.W. Fergus, K. Wang, C. Dela Cruz, Crystal Structure, Chemical Stabilities and Electrical Conductivity of Fe-Doped Manganese Cobalt Spinel Oxides for SOFC Interconnect Coatings, J. Electrochem. Soc. (2013). https://doi.org/10.1149/2.114311jes.

[9] Y. Zhou, S. Sun, J. Song, S. Xi, B. Chen, Y. Du, A.C. Fisher, F. Cheng, X. Wang, H. Zhang, Z.J. Xu, Enlarged Co□O Covalency in Octahedral Sites Leading to Highly Efficient Spinel Oxides for Oxygen Evolution Reaction, Adv. Mater. 30 (2018) 1–7. https://doi.org/10.1002/adma.201802912.

[10] R. Metz, J.P. Caffin, R. Legros, A. Rousset, The preparation, characterization and electrical

properties of copper manganite spinels, CuxMn3-xO4, 0 ≤x ≤ 1, J. Mater. Sci. 24 (1989) 83–87. https://doi.org/10.1007/BF00660936.

[11] G.T. Bhandage, H. V Keer, Structural and magnetic properties of the CuxCd1-xMn2O4 system, J. Phys. C Solid State Phys. 8 (1975) 501–506.

[12] G.T. Bhandage, H. V Keer, A correlation of the physical properties of the NixCu1-xMn2O4 system, J. Phys. C Solid State Phys. 9 (1976) 1325–1331.

[13] R. Buhl, Manganites spinelles purs d'elements de transition preparations et structures cristallographiques, J. Phys. Chem. Solids. 30 (1969) 805–812. https://doi.org/10.1016/0022-3697(69)90275-3.

[14] T. Fukunaga, N. Ryumon, N. Ichikuni, S. Shimazu, Characterization of CuMn-spinel catalyst for methanol steam reforming, Catal. Commun. 10 (2009) 1800–1803. https://doi.org/10.1016/j.catcom.2009.06.001.

[15] P. Ma, Q. Geng, X. Gao, T. Zhou, S. Yang, G. Liu, Aqueous solution-derived CuMn2O4 ceramic films for spectrally selective solar absorbers, Ceram. Int. (2016). https://doi.org/10.1016/j.ceramint.2016.09.062.

[16] J. Li, C. Xiong, J. Li, D. Yan, J. Pu, B. Chi, L. Jian, Investigation of MnCu0.5Co1.5O4spinel coated SUS430 interconnect alloy for preventing chromium vaporization in intermediate temperature solid oxide fuel cell, Int. J. Hydrogen Energy. 42 (2017). https://doi.org/10.1016/j.ijhydene.2017.05.074.

[17] F.C.M. Driessens, G.D. Rieck, Phase Equilibria in the System Cu-Mn-O, J. Inorg. Gen. Chem. 351 (1967) 48–62. https://doi.org/10.1002/zaac.19673510108.

[18] P. Wei, M. Bieringer, L.M.D. Cranswick, A. Petric, In situ high-temperature X-ray and neutron diffraction of Cu-Mn oxide phases, J. Mater. Sci. 45 (2010) 1056–1064. https://doi.org/10.1007/s10853-009-4042-2.

[19] C. Maunders, B.E. Martin, P. Wei, A. Petric, G.A. Botton, Investigation of the electronic structure of the cubic spinel Cu 1.2Mn1.8O4 using electron energy loss spectroscopy, Solid State Ionics. 179 (2008) 718–724. https://doi.org/10.1016/j.ssi.2008.04.029.

[20] B.E. Martin, A. Petric, Electrical properties of copper-manganese spinel solutions and their cation valence and cation distribution, J. Phys. Chem. Solids. (2007). https://doi.org/10.1016/j.jpcs.2007.06.019.

[21] P. Wei, Spinel coatings for Solid Oxide Fuel Cell interconnects and crystal structure of Cu-Mn-

O, McMaster University, Canada, 2009.

[22] A. Petric, H. Ling, Electrical conductivity and thermal expansion of spinels at elevated temperatures, J. Am. Ceram. Soc. (2007). https://doi.org/10.1111/j.1551-2916.2007.01522.x.

[23] Z. Sun, R. Wang, A.Y. Nikiforov, S. Gopalan, U.B. Pal, S.N. Basu, CuMn1.8O4 protective coatings on metallic interconnects for prevention of Cr-poisoning in solid oxide fuel cells, J. Power Sources. 378 (2018) 125–133. https://doi.org/10.1016/j.jpowsour.2017.12.031.

[24] Z. Sun, S. Gopalan, U.B. Pal, S.N. Basu, Cu1.3Mn1.7O4 spinel coatings deposited by electrophoretic deposition on Crofer 22 APU substrates for solid oxide fuel cell applications, Surf. Coatings Technol. 323 (2017) 49–57. https://doi.org/10.1016/j.surfcoat.2016.09.028.

[25] W. Huang, S. Gopalan, U.B. Pal, S.N. Basu, Evaluation of Electrophoretically Deposited CuMn[sub 1.8]O[sub 4] Spinel Coatings on Crofer 22 APU for Solid Oxide Fuel Cell Interconnects, J. Electrochem. Soc. (2008). https://doi.org/10.1149/1.2975367.

[26] P. Zielke, A.C. Wulff, X. Sun, S.H. Jensen, R. Kiebach, H.L. Frandsen, P. Norby, A. Hagen, Investigation of a Spinel-forming Cu-Mn Foam as an Oxygen Electrode Contact Material in a Solid Oxide Cell Single Repeating Unit, Fuel Cells. 17 (2017) 730–734. https://doi.org/10.1002/fuce.201700005.

[27] B. Talic, P.V. Hendriksen, K. Wiik, H.L. Lein, Thermal expansion and electrical conductivity of Fe and Cu doped MnCo2O4spinel, Solid State Ionics. 326 (2018) 90–99. https://doi.org/10.1016/j.ssi.2018.09.018.

[28] D. Szymczewska, S. Molin, P. Hendriksen, P. Jasiński, Microstructure and Electrical Properties of Fe,Cu Substituted (Co,Mn)3O4 Thin Films, Crystals. 7 (2017) 185. https://doi.org/10.3390/cryst7070185.

[29] T. Brylewski, A. Kruk, M. Bobruk, A. Adamczyk, J. Partyka, P. Rutkowski, Structure and electrical properties of Cu-doped Mn-Co-O spinel prepared via soft chemistry and its application in intermediate-temperature solid oxide fuel cell interconnects, J. Power Sources. 333 (2016) 145–155. https://doi.org/10.1016/j.jpowsour.2016.09.136.

[30] B. Talic, P.V. Hendriksen, K. Wiik, H.L. Lein, Thermal expansion and electrical conductivity of Fe and Cu doped MnCo2O4 spinel, Solid State Ionics. (2018). https://doi.org/10.1016/j.ssi.2018.09.018.

[31] S. Molin, P. Jasinski, L. Mikkelsen, W. Zhang, M. Chen, P. V. Hendriksen, Low temperature processed MnCo2O4 and MnCo1.8Fe0.2O4 as effective protective coatings for solid oxide fuel

cell interconnects at 750 °C, J. Power Sources. 336 (2016) 408–418. https://doi.org/10.1016/j.jpowsour.2016.11.011.

[32] E. Zanchi, B. Talic, A.G. Sabato, S. Molin, A.R. Boccaccini, F. Smeacetto, Electrophoretic co-deposition of Fe2O3 and Mn1,5Co1,5O4: Processing and oxidation performance of Fe-doped Mn-Co coatings for solid oxide cell interconnects, J. Eur. Ceram. Soc. 39 (2019). https://doi.org/10.1016/j.jeurceramsoc.2019.05.024.

[33] S. Molin, A.G. Sabato, H. Javed, G. Cempura, A.R. Boccaccini, F. Smeacetto, Co-deposition of CuO and Mn 1 . 5 Co 1 . 5 O 4 powders on Crofer22APU by electrophoretic method : Structural , compositional modifications and corrosion properties, Mater. Lett. 218 (2018) 329–333. https://doi.org/10.1016/j.matlet.2018.02.037.

[34] N. Grünwald, Y.J. Sohn, X. Yin, N.H. Menzler, O. Guillon, R. Vaßen, Microstructure and phase evolution of atmospheric plasma sprayed Mn-Co-Fe oxide protection layers for solid oxide fuel cells, J. Eur. Ceram. Soc. 39 (2019) 449–460. https://doi.org/10.1016/j.jeurceramsoc.2018.08.027.

[35] S. Joshi, A. Petric, Nickel substituted CuMn 2 O 4 spinel coatings for solid oxide fuel cell interconnects, Int. J. Hydrogen Energy. 42 (2017) 5584–5589. https://doi.org/10.1016/j.ijhydene.2016.08.075.

[36] M. Salavati-Niasari, F. Davar, M. Farhadi, Synthesis and characterization of spinel-type CuAl2O4 nanocrystalline by modified sol-gel method, J. Sol-Gel Sci. Technol. (2009). https://doi.org/10.1007/s10971-009-1940-3.

[37] J. Lin, Y. He, X. Du, Q. Lin, H. Yang, H. Shen, Structural and Magnetic Studies of Cr3+ Substituted Nickel Ferrite Nanomaterials Prepared by Sol-Gel Auto-Combustion, Crystals. 8 (2018) 384. https://doi.org/10.3390/cryst8100384.

[38] M. Bobruk, K. Durczak, J. Dąbek, T. Brylewski, Structure and Electrical Properties of Mn-Cu-O Spinels, J. Mater. Eng. Perform. 26 (2017) 1598–1604. https://doi.org/10.1007/s11665-017-2588-8.

[39] Z. Sun, S. Gopalan, U.B. Pal, S.N. Basu, Cu1.3Mn1.7O4 spinel coatings deposited by electrophoretic deposition on Crofer 22 APU substrates for solid oxide fuel cell applications, Surf. Coatings Technol. (2017). https://doi.org/10.1016/j.surfcoat.2016.09.028.

[40] M. Bobruk, K. Brylewska, K. Durczak, K. Wojciechowski, A. Adamczyk, T. Brylewski, Synthesis of manganese-cobalt spinel via wet chemistry methods and its properties, Ceram. Int. 43 (2017) 15597–15609. https://doi.org/10.1016/j.ceramint.2017.08.116.

[41] W. -S Hong, L.C. De Jonghe, X. Yang, M.N. Rahaman, Reaction Sintering of ZnO-AI2O3, J. Am. Ceram. Soc. (1995). https://doi.org/10.1111/j.1151-2916.1995.tb07957.x.

[42] J. Marín-Romero, L. Fuentes-Cobas, J. Rodríguez-Carvajal, C. Tabasco-Novelo, P. Quintana, Structure of a Novel Spinel Li0.5Zn5/3Sb2.5/3O4 by Neutron and Synchrotron Diffraction Analysis, Crystals. 7 (2017) 280. https://doi.org/10.3390/cryst7090280.

[43] A.E. Danks, S.R. Hall, Z. Schnepp, The evolution of “sol-gel” chemistry as a technique for materials synthesis, Mater. Horizons. (2016). https://doi.org/10.1039/c5mh00260e.

[44] M. Galceran, · M C Pujol, · M Aguiló, · F Díaz, M. Aguiló, F. Díaz, Sol-gel modified Pechini method for obtaining nanocrystalline KRE(WO4)2 (RE = Gd and Yb) Sol-gel modified Pechini method for obtaining nanocrystalline KRE(WO 4) 2 (RE = Gd and Yb), Artic. J. Sol-Gel Sci. Technol. 42 (2007) 79–88. https://doi.org/10.1007/s10971-006-1517-3.

[45] C.W. Bale, E. Bélisle, P. Chartrand, S.A. Decterov, G. Eriksson, A.E. Gheribi, K. Hack, I.H. Jung, Y.B. Kang, J. Melançon, A.D. Pelton, S. Petersen, C. Robelin, J. Sangster, P. Spencer, M.A. Van Ende, FactSage thermochemical software and databases, 2010-2016, Calphad Comput. Coupling Phase Diagrams Thermochem. 54 (2016) 35–53. https://doi.org/10.1016/j.calphad.2016.05.002.

[46] L.J. van der Pauw, A method of measuring the resistivity and Hall coefficient on samples of arbitrary shape, Philips Res. Reports. (1958). https://doi.org/537.723.1:53.081.7+538.632:083.9.

[47] R. Landauer, Electrical conductivity in inhomogeneous media, in: AIP Conf. Proc., AIP Publishing, 2008: pp. 2–45. https://doi.org/10.1063/1.31150.

[48] A. Purwanto, A. Fajar, H. Mugirahardjo, J.W. Fergus, K. Wang, Cation distribution in spinel (Mn,Co,Cr)3O4 at room temperature, J. Appl. Crystallogr. 43 (2010) 394–400. https://doi.org/10.1107/S0021889810008150.

[49] H.A. Jahn, E. Teller, Stability of polyatomic molecules in degenerate electronic states - I—Orbital degeneracy, Proc. R. Soc. 161 (1937) 220–235.

[50] J.D. Dunitz, L.E. Orgel, Electronic properties of transition-metal oxides—I. Distrortions from cubic symmetry, J. Phys. Chem. Solids. 3 (1957) 20–29. https://doi.org/10.1016/0022-3697(57)90043-4.

[51] N. Baffier, M. Huber, Etude par diffraction des rayons X et des neutrons, des relations entre distribution cationique et distorsion cristalline dans les ferro-manganites spinelles: xMn3O4 +

(1 - x) Cu(Fe,Cr)2O4, J. Phys. Chem. Solids. 33 (1972) 737–747. https://doi.org/10.1016/0022-3697(72)90081-9.

[52] Y. Zhu, K. Mimura, M. Isshiki, Oxidation mechanism of Cu2O to CuO at 600-1050 °C, Oxid. Met. 62 (2004) 207–222. https://doi.org/10.1007/s11085-004-7808-6.

[53] T. Narushima, H. Tsukamoto, T. Yonezawa, High temperature oxidation event of gelatin nanoskin-coated copper fine particles observed by in situ TEM, AIP Adv. 2 (2012). https://doi.org/10.1063/1.4759498.

[54] N. Ponpandian, P. Balaya, A. Narayanasamy, Electrical conductivity and dielectric behaviour of nanocrystalline $NiFe_2O_4$ spinel, J. Phys. Condens. Matter. 14 (2002) 3221–3237. https://doi.org/10.1088/0953-8984/14/12/311.

[55] M. Stygar, K. Matsuda, S. Lee, T. Brylewski, Corrosion Behavior of Crofer 22APU for Metallic Interconnects in Single and Dual Atmosphere Exposures at 1073 K, 131 (2017). https://doi.org/10.12693/APhysPolA.131.1394.

[56] Stainless Steel Type 441 – Rolled Metal Products | Stainless, Aluminum & Specialty Alloys, (n.d.). https://rolledmetalproducts.com/stainless-steel-type-441/ (accessed March 9, 2020).

[57] C. Goebel, A.G. Fefekos, J.E. Svensson, J. Froitzheim, Does the conductivity of interconnect coatings matter for solid oxide fuel cell applications?, J. Power Sources. 383 (2018) 110–114. https://doi.org/10.1016/j.jpowsour.2018.02.060.

[58] M. Bobruk, S. Molin, M. Chen, T. Brylewski, P. V. Hendriksen, Sintering of MnCo2O4coatings prepared by electrophoretic deposition, Mater. Lett. (2018). https://doi.org/10.1016/j.matlet.2017.12.046.